Rupture parameters of the 2003 Zemmouri (M_w 6.8), Algeria, earthquake from joint inversion of interferometric synthetic aperture radar, coastal uplift, and GPS

Samir Belabbès,[1] Charles Wicks,[2] Ziyadin Çakir,[3] and Mustapha Meghraoui[1]

[1]   We study the surface deformation associated with the 21 May 2003 ($M_w = 6.8$) Zemmouri (Algeria) earthquake, the strongest seismic event felt in the Algiers region since 1716. The thrust earthquake mechanism and related surface deformation revealed an average 0.50 m coastal uplift along ~55-km-long coastline. We obtain coseismic interferograms using Envisat advanced synthetic aperture radar (ASAR) (IS2) and RADARSAT standard beam (ST4) data from both the ascending and descending orbits of Envisat satellite, whereas the RADARSAT data proved useful only in the descending mode. While the two RADARSAT interferograms cover the earthquake area, Envisat data cover only the western half of the rupture zone. Although the interferometric synthetic aperture radar (InSAR) coherence in the epicenter area is poor, deformation fringes are observed along the coast in different patches. In the Boumerdes area, the maximum coseismic deformation is indicated by the high gradient of fringes visible in all interferograms in agreement with field measurements (tape, differential GPS, leveling, and GPS). To constrain the earthquake rupture parameters, we model the interferograms and uplift measurements using elastic dislocations on triangular fault patches in an elastic and homogeneous half-space. We invert the coseismic slip using first, a planar surface and second, a curved fault, both constructed from triangular elements using Poly3Dinv program that uses a damped least square minimization. The best fit of InSAR, coastal uplift, and GPS data corresponds to a 65-km-long fault rupture dipping 40° to 50° SE, located at 8 to 13 km offshore with a change in strike west of Boumerdes from N60°–65° to N95°–105°. The inferred rupture geometry at depth correlates well with the seismological results and may have critical implications for the seismic hazard assessment of the Algiers region.

1. Introduction

[2]   The thrust and fold system of the Tell Atlas (northern Algeria) has been the site of several large and moderate earthquakes in the last decades (Table 1). This shallow seismic activity was very often associated with surface faulting, the conspicuous example being the El Asnam thrust faulting and related 1980, M_w 7.3 major event [*Philip and Meghraoui*, 1983; *Yielding et al.*, 1989]. The thrust mechanism (global centroid moment tensor (CMT)) of the M_w 6.8, 2003 Zemmouri earthquake which occurred in the Tell Atlas tectonic belt, confirms the pattern of active deformation that predicts 4–6 mm/a of convergence along the Africa-Eurasia plate boundary (Figure 1a) [*Meghraoui et al.*, 1996; *Nocquet and Calais*, 2004; *Serpelloni et al.*, 2007]. Its coastal location hindered, however, the direct observation of surface ruptures and has left open questions on the probable fault scarp location, structural characteristics and geometry of the causative fault [*Meghraoui et al.*, 2004; *Déverchère et al.*, 2005].

[3]   The 2003 Zemmouri earthquake (also called sometimes the Boumerdes earthquake) affected the eastern edge of the Mitidja Quaternary basin (Figure 1b), and was responsible for severe damage ~20 km east of the capital city Algiers [*Ayadi et al.*, 2003; *Harbi et al.*, 2007]. The NE-SW striking fault is consistent with the Tell Atlas fold and thrust tectonics, the uplifted 55-km-long coastal shoreline [*Meghraoui et al.*, 2004], the ~40° SE dipping aftershocks [*Ayadi et al.*, 2008] and the inversion of body waves [*Delouis et al.*, 2004; *Yagi*, 2003]. A detailed bathymetric survey and seismic profiles offshore describe the morphological and structural features in the Mediterranean Sea [*Domzig et al.*, 2006]. A downdip model of uniform slip

[1]Institut de Physique du Globe de Strasbourg, UMR 7516, Strasbourg, France.
[2]U.S. Geological Survey, Menlo Park, California, USA.
[3]Faculty of Mines, Istanbul Technical University, Istanbul, Turkey.

Table 1. Large and Moderate Earthquakes With Thrust Mechanism Along the Tell Atlas

Location	Date	Longitude (deg)	Latitude (deg)	M_w
Orléansville	9 Sep 1954	1.47	36.28	6.7
El Asnam	10 Oct 1980	1.36	36.18	7.3
Tipaza	29 Oct 1989	2.92	36.84	5.9
Mascara	18 Aug 1994	−0.03	35.40	5.7
Ain Temouchent	22 Dec 1999	−1.45	35.34	5.7
Beni Ourtilane	10 Nov 2000	4.69	36.71	5.7
Zemmouri	21 May 2003	3.65	36.83	6.8

on a rectangular dislocation deduced from direct measurements of coastal uplift (using differential GPS (DGPS) and conventional leveling [*Meghraoui et al.*, 2004]) is consistent with the slip distribution at depth inferred from the inversion of seismic and geodetic data [*Delouis et al.*, 2004]. These models of seismic source include surface slip and comply with the observed tsunami effects and related tide gauge records in the western Mediterranean Sea [*Alasset et al.*, 2006].

[4] The analysis of SAR images and related interferograms in the last decade has led to a significant progress in the understanding of earthquake deformation [*Massonnet and Feigl*, 1998; *Bürgmann et al.*, 2000; *Wright et al.*, 2004]. The phase interference of spaceborne radar images has the outstanding advantage to locate and display the field displacement of large sections of any earthquake area, providing that an appropriate coherence level exists between SAR images. The generation of SAR interferograms is therefore particularly important in thrust and fold systems with complex surface deformation (seismic and aseismic) [*Fielding et al.*, 2004] as it may lead to a better seismic hazard assessment. The application of interferometric synthetic aperture radar (InSAR) in active zones of North Africa has been recently performed for the M_w 5.7, 1999 Ain Temouchent blind thrust earthquake [*Belabbes et al.*,

2008] and for the M_w 6.0, 1994 and M_w 6.4, 2004 Al Hoceima earthquakes which revealed the existence of blind and conjugate seismic ruptures in the Rif Mountain belt [*Cakir et al.*, 2006; *Akoglu et al.*, 2006] (Figure 1a). The coastal location of the Zemmouri earthquake is not an ideal configuration for producing interferograms since most of the earthquake deformation occurred offshore. Nevertheless, the impressive coastal uplift and epicenter location imply that significant surface deformation took place inland as well and can be studied using SAR images.

[5] In this paper, we first present the seismotectonic characteristics of the Zemmouri earthquake and provide a detailed study of interferograms obtained from RADARSAT and Envisat images. The InSAR data document the measurements of displacement field in the earthquake area in agreement with previous studies of coastal uplift. Modeling of the InSAR data set together with the uplift and GPS measurements allow us to deduce the fault parameters and associated coseismic slip distribution. Finally, open questions on the earthquake fault geometry and the importance of InSAR analysis are discussed emphasizing the constraint of a hidden seismogenic thrust rupture with coastal geodetic, tectonic and seismologic data.

2. Seismotectonic Setting

[6] The Tell Atlas of northern Algeria experienced the largest recorded earthquake at El Asnam (10 October 1980, M_w 7.3) related to a NE-SW trending reverse fault [*Ouyed et al.*, 1981; *Philip and Meghraoui*, 1983]. Other recent large and moderate seismic events of this region (Figures 1a and 1b and Table 1), including the Zemmouri earthquake of 2003 revealed a comparable pattern of active deformation in agreement with the NNW-SSE to NW-SE convergence and transpressive tectonics along the Africa-Eurasia plate boundary [*Meghraoui et al.*, 1996; *Stich et al.*, 2003]. These seismogenic structures of the Tell Atlas are related to a
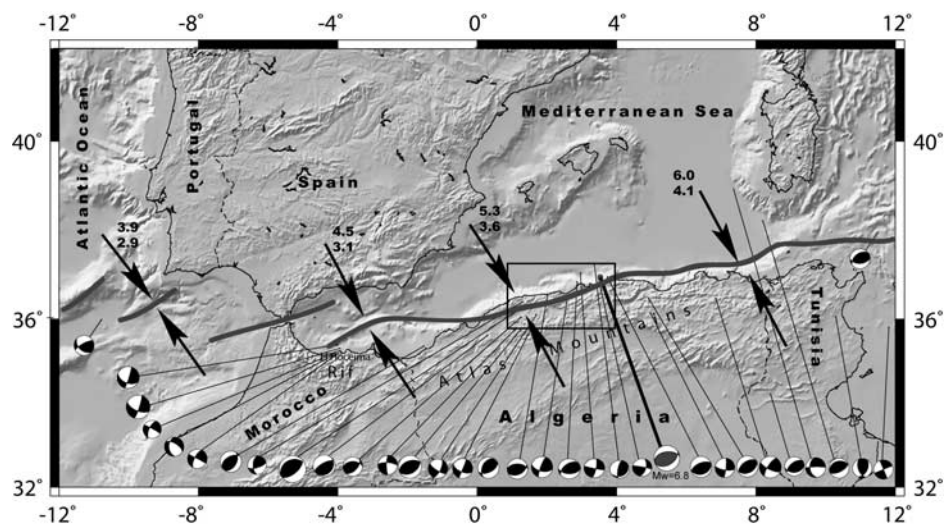

Figure 1a. Shaded relief map of eastern Mediterranean with focal mechanism solutions of earthquakes between 1980 and 2005 (data from Global CMT catalog). Gray mechanism corresponds to the 2003 Zemmouri earthquake. The gray line represents the plate boundary according to *Meghraoui et al.* [1996]. Black arrows are direction of convergence, and the number is plate velocity in mm/a [*Nocquet and Calais*, 2004]. The squared area is for Figure 1b.
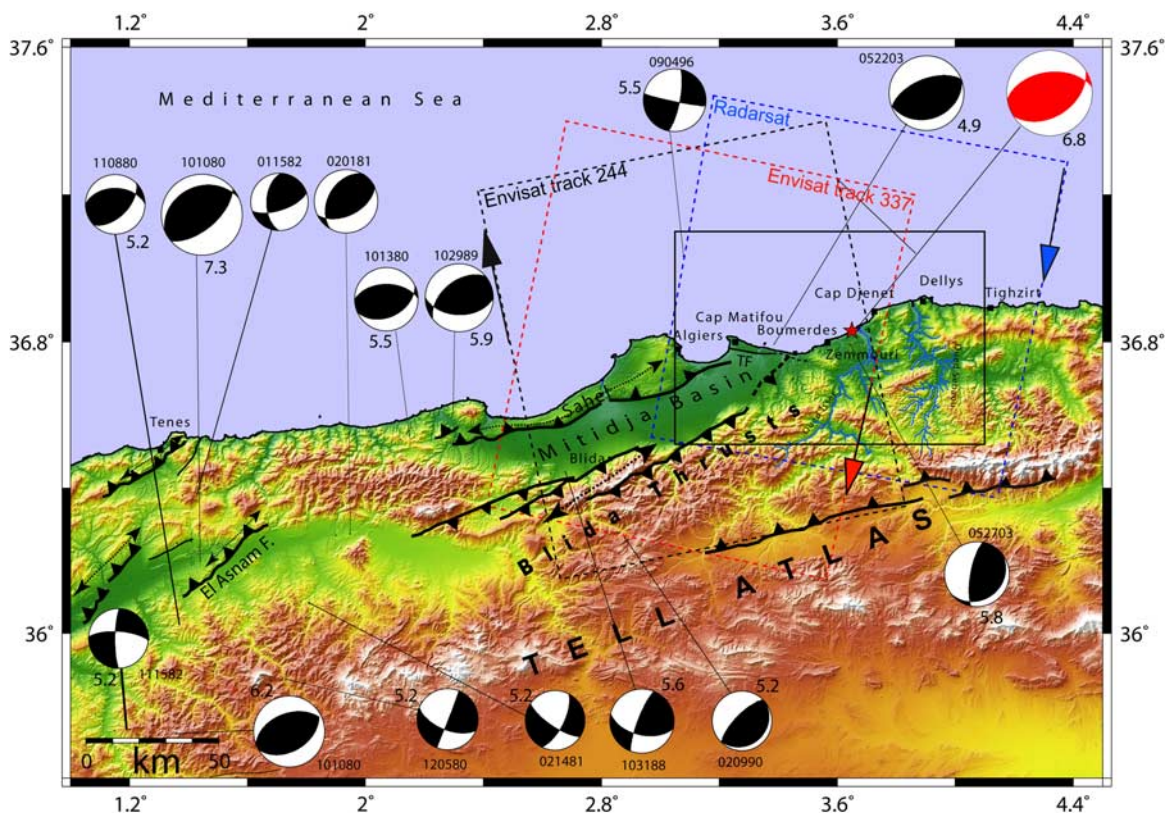
Figure 1b. Envisat/RADARSAT radar frames (dashed rectangles) with arrows indicating the satellite flight direction for ascending and descending orbits of the 21 May 2003 Zemmouri earthquake area. Red, black, and blue arrows indicate flight direction for satellites. The red star indicates the earthquake epicenter location [*Bounif et al.*, 2004], and focal mechanisms are from the Global CMT solution between 1980 and 2003 (size of beach balls is according to magnitude and red mechanism is for the Zemmouri earthquake). Black lines indicate active thrust faults, and dashed arrowed lines indicate active folding and west of the 2003 epicenter TF is for Thenia Fault [*Meghraoui*, 1988].

complex "en echelon" thrust and fold system located along an E-W trending narrow strip parallel to the coastline. The late Quaternary active deformation that indicates a rate of 2 to 3 mm/a. for compressive movements estimated from the shortening of folded units and paleoseismic investigations [*Meghraoui and Doumaz*, 1996], is comparable to the 4 to 6 mm/a. convergence rate obtained from NUVEL-1A and global GPS solutions along the plate boundary [*Nocquet and Calais*, 2004; *Serpelloni et al.*, 2007].

[7] The 2003 Zemmouri earthquake affected ~55-km-long coastline and ~15-km-thick uppermost crustal structure that belongs to the eastern regions of the Mitidja Basin and related Blida thrust and fold system [*Ayadi et al.*, 2008]. A detailed study of the main shock relocation [*Bounif et al.*, 2004] and aftershock distribution (that covers 2 months) using the tomography analysis reveals a NE-SW trending and 40°SE dipping fault zone with two seismicity patches [*Ayadi et al.*, 2008]. The double difference seismic analysis shows a large concentration of aftershocks and depth distribution SW of the fault rupture and indicates a SE dipping thrust geometry in agreement with the centroid moment tensor (CMT) solution (Figure 2 and Table 2) [*Ayadi et al.*, 2008]. Using an analysis of body waves and surface waves of teleseismic records, *Delouis et al.* [2004] found 2.86 × 10^{19} N m seismic moment and a ~15 s fault

rupture with ~1 m surface slip, and 2.1 m maximum slip at depth with bilateral rupture propagation along two patches (Table 2). *Yagi* [2003] also constructed source models from body wave inversion and obtained similar results pointing out the bilateral rupture propagation on a 60-km-long fault with 2 patches and 2.3 m maximum slip at depth (Table 2). The inversion of geodetic data (coastal uplift and GPS) and accelerograms also points out the two patches with up to 1 m surface slip SW of the earthquake rupture [*Semmane et al.*, 2005]. According to the fault geometry, seismic moment, main shock location at depth and field observations, the earthquake fault did not rupture the surface along the coastline but likely offshore at the seafloor. Detailed field investigations made immediately after the main shock indicate, however, the existence of 2- to 3-km-long N95°–100° trending surface cracks observed along the Thenia fault (Figure 1b).

[8] Coseismic uplift of marine terraces along the 55-km-long coastline (Figure 3) combined with GPS and conventional leveling indicate an average of 0.55 m vertical movement with two slip patches from which a SE dipping planar dislocation model is resolved with 2.8 × 10^{19} N m geodetic moment [*Meghraoui et al.*, 2004]. Although based on a 60-km-long and 15-km-wide simple rectangular dislocation, the model suggests a seismogenic thrust rupture
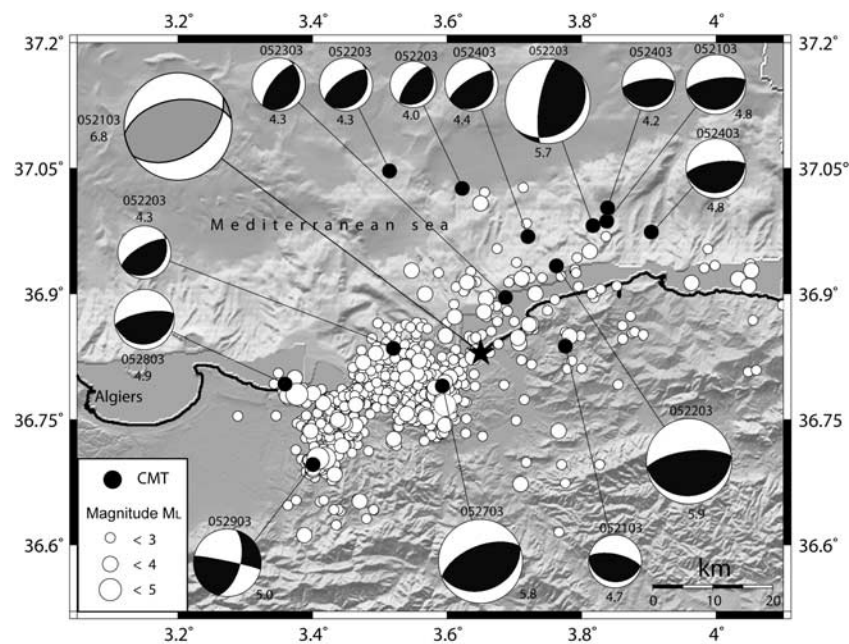
Figure 2. The 21 May 2003 Zemmouri earthquake (black star, M_w 6.8) and aftershock distribution (white circles) of seismic events from 25 May to 31 July 2003 [*Ayadi et al.*, 2008]. The main shock and main aftershocks (black circles) are relocated using the double difference seismic analysis of *Bounif et al.* [2004]. Focal mechanism solutions are Global CMT.

dipping 50° SE consistent with the seismological results (Table 2). The coastal deformation and rupture history associated with the aftershock distribution (Figure 2), showing a clear concentration of seismic events on the SW patch suggest, however, a complex fault rupture likely made of several asperities along strike. Early results from geodetic measurements (coastal uplift and GPS) and seismicity analysis [*Bounif et al.*, 2004; *Meghraoui et al.*, 2004; *Delouis et al.*, 2004; *Yelles et al.*, 2004; *Semmane et al.*, 2005; *Alasset et al.*, 2006] imply the existence of a N54°–N70° striking and 40° to 50° SE dipping fault plane with surface slip at 5 to 15 km offshore. From the high-resolution swath bathymetry and seismic profiles *Déverchère et al.* [2005] study the seafloor of the continental slope offshore the 2003 earthquake area, identify outcropping thrust fault and scarps located at ∼20 and 32 km from the shoreline and infer a flat and ramp rupture geometry. The moment tensor analysis obtained from broadband seismic records yields a

25° SE dipping rupture (Table 2) that suggests a fault surface trace at 15 to 20 km offshore limited to the SW by a NNE trending transform fault and forms a step over with the Blida thrust system [*Braunmiller and Bernardi*, 2005].

3. The InSAR Analysis

[9] We have calculated four coseismic interferograms, one ascending and three descending, using synthetic aperture radar (SAR) data acquired by the Canadian Space Agency's RADARSAT satellite and European Space Agency's Envisat satellite (Table 3). The raw data were processed using the commercial GAMMA software with 5 azimuth 1 range look (i.e., averaged to 20 × 20 m of ground pixel size) and filtered using weighted power spectrum technique of *Goldstein and Werner* [1998]. The effect of topography that depends on the perpendicular separation between orbital trajectories is

Table 2. Fault Plane Parameters of the 21 May 2003 Zemmouri Earthquake

Source	Longitude (deg)	Latitude (deg)	Depth (km)	Plane 1[a]			Plane 2			M_0 (N m)
				Strike (deg)	Dip (deg)	Rake (deg)	Strike (deg)	Dip (deg)	Rake (deg)	
HRV	3.58	36.93	15	57	44	71	262	49	107	2.01×10^{19}
USGS	3.78	36.89	9	54	47	88	237	43	92	1.30×10^{19}
INGV	3.61	36.9	15	65	27	86	250	63	92	1.80×10^{19}
Yagi [2003]	3.65[b]	36.83[b]	-	54	47	86	-	-	-	2.40×10^{19}
Delouis et al. [2004]	3.65[b]	36.83[b]	-	70	40	95	-	-	-	2.80×10^{19}
Meghraoui et al. [2004]	3.65[b]	36.83[b]	-	54	50	88	-	-	-	2.75×10^{19}
Braunmiller and Bernardi [2005]	3.65[b]	36.83[b]	-	62	25	82	-	-	-	3.48×10^{19}
This study planar model	3.65[b]	36.83[b]	8	65	40	90	-	-	-	1.78×10^{19}
This study curved model	3.65[b]	36.83[b]	10	65	40	90	-	-	-	2.15×10^{19}

[a]Plane 1 is the principal fault according to field observations.
[b]Epicenter relocation by *Bounif et al.* [2004].

Figure 3. Coastal uplift at 6 km west of Dellys (Figure 1b). The photograph shows the elevated marine terrace and platform (black arrow is the former shoreline and white arrow is the new shoreline) with an average 0.55 m of uplift [*Meghraoui et al.*, 2004].

removed from the interferograms using the SRTM 3-arc-sec (∼90 m) posting digital elevation model [*Farr et al.*, 2007]. Envisat interferograms were obtained using precise orbits from Delft University [*Scharroo and Visser*, 1998] while for RADARSAT interferograms orbital information are from the data header.

[10] Baselines for Envisat data were not reestimated because there are no orbital residuals visible farther south of the earthquake area where there is supposedly no surface deformation. The available RADARSAT orbits are imprecise and processing them leaves orbital errors. Therefore, we have modeled the orbital residuals with a 2-D quadratic surface and subtracted it from the interferograms [*Zebker et al.*, 1994].

[11] While the descending RADARSAT frame covers entirely the uplifted coastal region from Cap Matifou to the west and Tighzirt to the east, both the ascending and descending Envisat frames cover only the western part of the earthquake area (Figure 1b). Despite the atmospheric noise and low coherence particularly in the epicentral area, the interferograms display clear coseismic fringes all along the coast (Figure 4). The poor coherence in the epicentral

region exists in all the interferograms and is most likely due to the high agricultural activity along the Oued Isser River. Signal decorrelation in the Envisat interferograms also occurs to the south in the mountainous regions due to the low altitude of ambiguity of the interferometric pairs (Table 3). Because of the significant change in the look direction (Table 4), the interferograms naturally differ from each other. However, the difference is not remarkable since the deformation is overwhelmingly vertical, which can also be seen in Figures 4e, 4f, and 4g that show digitized fringes of all interferograms. The difference in the fringe pattern between the interferograms is mostly due to the horizontal component of the surface displacement. RADARSAT interferograms indicate that there are two lobes of deformation centered in the Boumerdes and Cap Djenet regions with the earthquake epicenter being located in the area of lower deformation in between them (Figures 4a and 4b). All interferograms indicate that the maximum surface deformation occurred indeed in the Zemmouri-Boumerdes region, confirming the field measurement of the coastal uplift [*Meghraoui et al.*, 2004]. In this region, up to 14 fringes can be counted in the RADARSAT interferograms

Table 3. Characteristics of SAR Images Covering the 2003 Zemmouri Earthquake Area

Satellite	Beam Mode	Master Orbit	Master Date	Slave Orbit	Slave Date	Trajectory	Altitude of Ambiguity (m)	B perp (m)
RADARSAT1	ST4	35996	27 Sep 2002	40798	29 Aug 2003	Descending	1358	12
RADARSAT1	ST4	35996	27 Sep 2002	41141	22 Sep 2003	Descending	84	194
Envisat	IS2	4900	6 Feb 2003	6904	26 Jun 2003	Descending	22	238
Envisat	IS2	5308	6 Mar 2003	7312	24 Jul 2003	Ascending	40	419
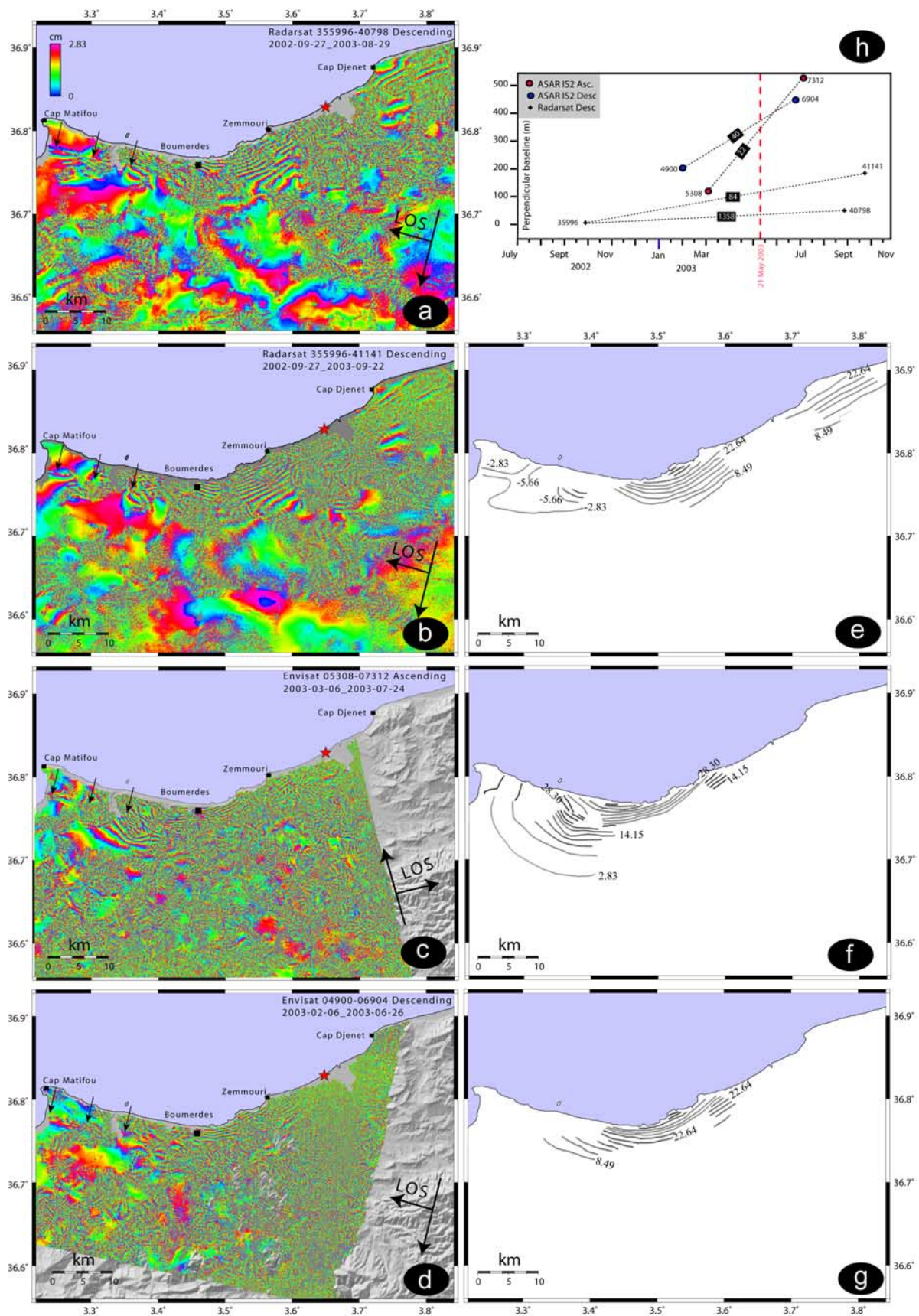
Figure 4

Table 4. Unit Vectors of SAR Scenes

Satellite	Flight Direction	East	North	Up
RADARSAT	Descending	0.59339	−0.10980	0.79739
Envisat	Descending	0.37188	−0.07946	0.92487
Envisat	Ascending	−0.38526	−0.08173	0.91918

(Figures 4a and 4b) and 16 fringes in the Envisat interferograms (Figures 4c and 4d). Assuming purely vertical deformation, these line-of-sight (LOS) displacements correspond approximately to 0.50 m of uplift since the Envisat interferograms are more sensitive to vertical deformation than the RADARSAT interferograms. Captured only by the RADARSAT interferograms, the LOS displacement in the Cap Djenet region reaches to ~0.25 m (i.e., 9 fringes).

[12] An examination of interferograms reveals some anomalies in the fringe pattern of the Cap Matifou region (black arrows in Figure 4). Fringes are clearly disturbed, offset and inverted along a lineament that coincides with the Thenia fault. This implies that the Thenia fault must have experienced some triggered slip during or after the main shock, a phenomenon commonly observed due to large earthquakes [Fialko et al., 2002].

4. Modeling the InSAR Data

[13] We used the Poly3Dinv slip inversion method to model geodetic data using realistic fault surfaces (see also maps in Figures 5a and 5b) [Thomas, 1993; Maerten et al., 2005]. The method is based on the analytical solution for a triangular dislocation in a linear, elastic, homogeneous and isotropic half-space, which uses triangular surfaces as discontinuities [Maerten et al., 2005]. Hence, the use of triangular elements allowed us to construct fault models that better approximate two-dimensional planar surfaces, avoiding gaps and overlaps that are inevitably encountered when modeling highly segmented faults of varying strike with simple rectangular dislocations. This method improves the fit to the geodetic data particularly in the near field when modeling complicated fault ruptures [Maerten et al., 2005; Resor et al., 2005]. Fault surfaces meshed with triangles were constructed using MATLAB®. We meshed the planar offshore fault with 6 × 5 quadrangles (i.e., 60 triangles) and 2 × 1 quadrangles for the Thenia fault. The slip distribution of the triangle elements was then inverted for, with a negativity constraint on the dip slip component (i.e., thrust only, 90° rake). To avoid unphysical oscillatory slip, the scale-dependent umbrella smoothing operator of Poly3Dinv is applied to the inverted slip distribution. We choose the smoothing factor based on the RMS misfit versus roughness

curve; this selected factor (i.e., 0.4) represents the best compromise between the roughness of slip and misfit to the data (Figures 5a and 5b). In our inversions, we use digitized fringes because some of them cannot be unwrapped due to noise and unwrapping errors. In this case, the residual interferograms are obtained by a multiplication in the complex domain of the data and the synthetic interferograms. On the basis of the fringe gradient, the southernmost fringe in the isolated patch located near Cap Djenet (Figure 4e) is assumed to be the third fringe (i.e., 8.49 cm) and the large curved fringe southeast of Boumerdes (Figure 4f) is assumed to be the first fringe (i.e., 2.83 cm). A constant offset in the InSAR data is not solved as we think it is negligible since one may observe to the south areas of nominal deformation.

[14] In order to constrain the location and geometry of the fault rupture, we run several inversions using digitized fringes (Figures 4e, 4f, and 4g), coastal uplift measurements [Meghraoui et al., 2004] and coseismic GPS vectors [Yelles et al., 2004]. The InSAR, coastal uplift and GPS data were treated as equally weighted in all inversions. The Poisson ratio in the elastic half-space is given as 0.25. A tilt for orbital residuals is solved by the Poly3D inversion but found to be insignificant. Several attempts with no constraints on the fault rake are performed but the inversion predicts abnormally high strike-slip (both right and left lateral) components. Therefore, we keep the N60°−65° strike and rake as pure thrust (90°) fixed and test several fault plane dips (20°−60°) in agreement with most of focal mechanism parameters of the 2003 main shock (Table 2). In the absence of any observed seafloor rupture and related SAR data, no surface slip on the uppermost patches is allowed in the inversions. However, it is possible that some slip reached the seafloor, but neither the SAR data nor the uplift measurements can resolve it. Taking into account the surface deformation and seismotectonic framework of the epicentral area, we suggest the following two slip models:

[15] 1. A variable slip model is obtained using inversions with various planar faults striking N65° and dipping 30°, 40°, and 50° SE located from 6 km to 24 km offshore (Figure 5a). The best fitting model (RMS = 2.69 cm) is obtained with 60-km-long and 30-km-wide offshore thrust fault (i.e., fault 4 in Figure 5a) striking N65°, dipping 30° to 40° SE and located at ~13 km offshore from the epicenter (Figures 5a and 6a). However, as illustrated in the RMS versus distance plot of Figure 5a, the fault tip location is not tightly constrained and could be anywhere between 9 to 18 km from the shoreline. The best fitting model predicts a coseismic slip distribution at ~8- to 10-km-depth on the

Figure 4. Coseismic interferograms of the western deformation zone of the 2003 Zemmouri earthquake area in (a and b) the descending RADARSAT geometry and (c and d) ascending and descending Envisat radar geometry; the image reference (date and orbit numbers) is in the top right corner. Black arrows indicate the satellite flight direction. Star shows the 2003 Zemmouri earthquake epicenter [Bounif et al., 2004]. (e, f, and g) Digitized fringes labeled with displacement (in cm) in the line-of-sight (LOS) direction for each interferogram (Figure 4e with 4b, Figure 4f with 4c, and Figure 4g with 4d). (h) baselines with altitudes of ambiguity in m (in black box) for each pair of SAR images with orbit numbers. Fringes are observed in all interferograms with 2 lobes of high deformation centered in Boumerdes and Cap Djenet region. N105° trending black arrows near Cap Matifou show the anomalies observed in the fringe pattern along the Thenia Fault (Figure 1b). The western earthquake area between Cap Matifou and Zemmouri shows several fringes that correspond to the zone of maximum deformation.

fault and shows two linked asperities reaching 4.7 m and ~3 m maximum slip in the NE and SW patches, respectively, and 1.78×10^{19} N m (M_w 6.8) geodetic moment. Additionally, offset fringes observed along the Thenia Fault

(TF in Figure 1b) in Cap Matifou are modeled in a forward manner with a 0.38 m slip on a ~20-km-long subvertical right-lateral fault as the inversions fail to explain the disturbed fringes (Figure 4).
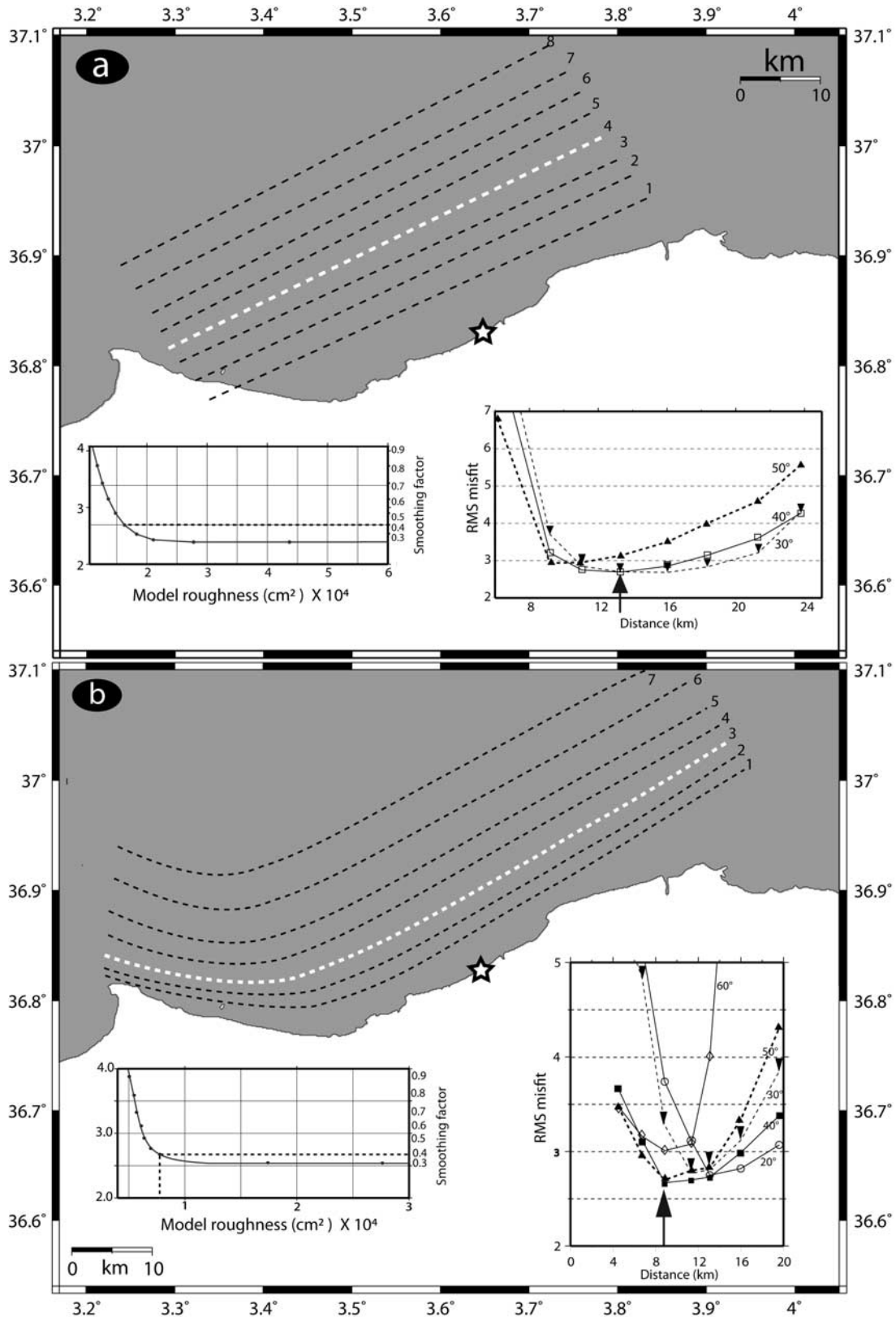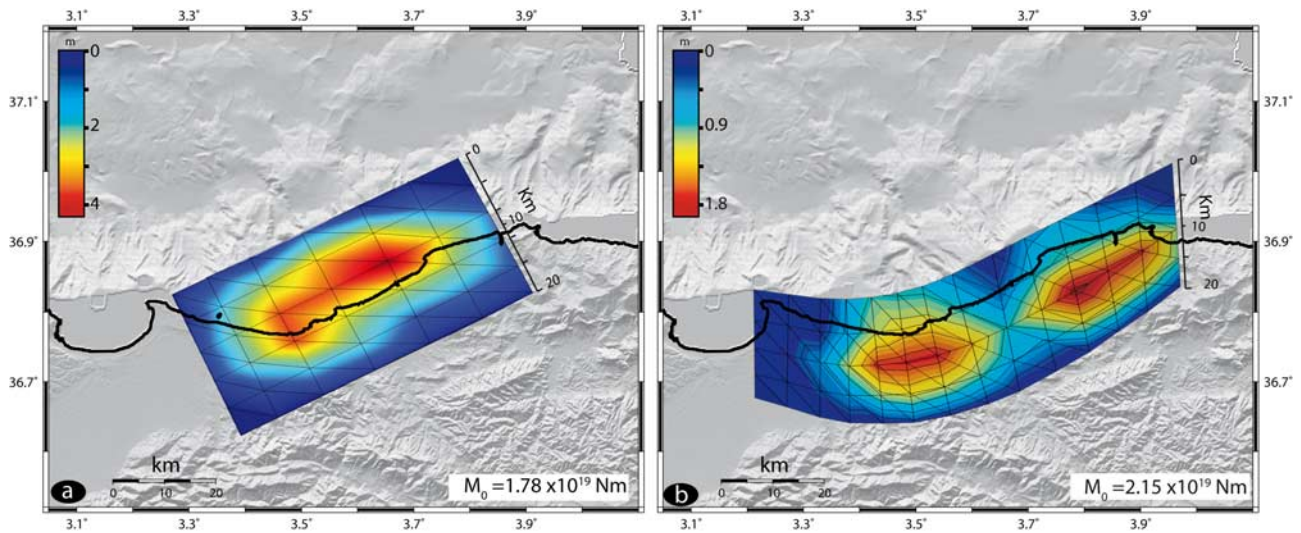

Figure 5

Figure 6. (a) Slip distribution model of preferred planar fault (4 in Figure 5a) of the Zemmouri earthquake rupture obtained from the inversion of the digitized fringes and coastal uplift data. Dip component of the coseismic slip on each triangular element are inverted using Poly3Dinv. Dip-slip distribution (4.7 m maximum from colored contours on fault surfaces) shows two linked maximum of slip on the N65° trending and 60-km-long major fault rupture. (b) Slip distribution of the preferred curved fault model striking N60° (∼65 km) to N102° (∼13 km) on the western part. The curved fault model is constructed with Poly3D in order to match the two fault planes with different strikes. Dip-slip distribution (2.1 m maximum from colored contours) with two distinct maximum slips reaching the seafloor north of Boumerdes and Cap Djenet.

[16] 2. The alternative model takes into account the complicated fringe distribution west of Boumerdes (Figures 4a, 4b, 4c, and 4d) and also includes the inversion of coseismic slip on regularly spaced faults (∼2 km) from 4 to 20 km offshore (Figure 5b). To the NE, faults are planar with an azimuth of N60–65°, consistent with the aftershocks distribution [*Ayadi et al.*, 2008] and focal mechanism solutions of the main shock (Table 2). The SW fault section is modeled according to the N95°–105° trending aftershocks and related tomography [*Ayadi et al.*, 2008] where the main NE-SW trending earthquake rupture cannot crosscut the continuous fringes visible particularly in the ascending Envisat interferogram west of Boumerdes (Figure 4c). This change in fault strike may be modeled as a curved fault. The slip on each fault is inverted for dips 20°, 30°, 40°, 50° and 60° SE using the same InSAR, GPS, and coastal uplift data. As shown in Figure 5b, the inversion results suggest that the minimum RMS misfits improve the fault location between 8 and 13 km offshore. The lowest 2.67 cm RMS error indicates that the fault rupture is most probably located

between 8 and 9 km offshore (from the epicenter) for a fault dipping 40° and 50° SE. The RMS misfit plot also shows minimum values (2.77 cm, 2.81 cm) for 30° SE dipping fault at 11 km offshore and for 20°, 30°, 40°, and 50° at 13 km offshore (Figure 5b). Taking into account the 40° to 50° SE fault dip of most focal mechanism solutions (Table 2) and the 40° SE dipping fault geometry from aftershocks tomography analysis [*Ayadi et al.*, 2008], we select fault 3 in Figure 5b with 40° to 50° SE dip as our preferred solution. The fault is here a 65-km-long and 30-km-wide offshore thrust fault striking N65° and dipping 40° SE, to the nearly vertical and ∼N102° trending rupture SW of the epicenter (Figure 5b). Two distinct slip patches yield 2.15×10^{19} N m (M_w 6.8) geodetic moment with ∼0.5 m slip reaching the seafloor (Figure 6b). Additionally, offset fringes observed in Cap Matifou (Figures 4a, 4b, 4c, and 4d) may be explained by 0.15 m triggered slip on the 20-km-long subvertical right-lateral secondary Thenia fault (Figure 1b).

[17] Figure 7 shows the synthetic interferograms predicted by the best fitting models with planar (Figures 7a–

Figure 5. (a) Map of the different planar fault tip positions (1 to 8) used for the inversions. The white star represents the main shock epicenter [*Bounif et al.*, 2004] and the reference point for distance calculation. Note that fault 4 (white dashed line) represents in this case the preferred fault model taking into account the lowest RMS misfit (right inset). The right inset shows the RMS error versus distance from the epicenter for different faults (1 to 8) with various dips (30°, 40° and 50°). The arrow shows the preferred solution at ∼13 km. The left inset shows the model roughness versus the RMS misfit, the corresponding smoothing factor for each model roughness is indicated on the right axis. (b) Map of different curved fault tip positions (dashed lines) used for the inversion with various dips (20°, 30°, 40°, 50° and 60°). The lowest RMS error is calculated for the 40° and 50° curved fault at ∼9 km (white dashed line 3) from the epicenter and represents our preferred model. The right inset shows the RMS misfit versus the model roughness with 0.4 corresponding smoothing factor.
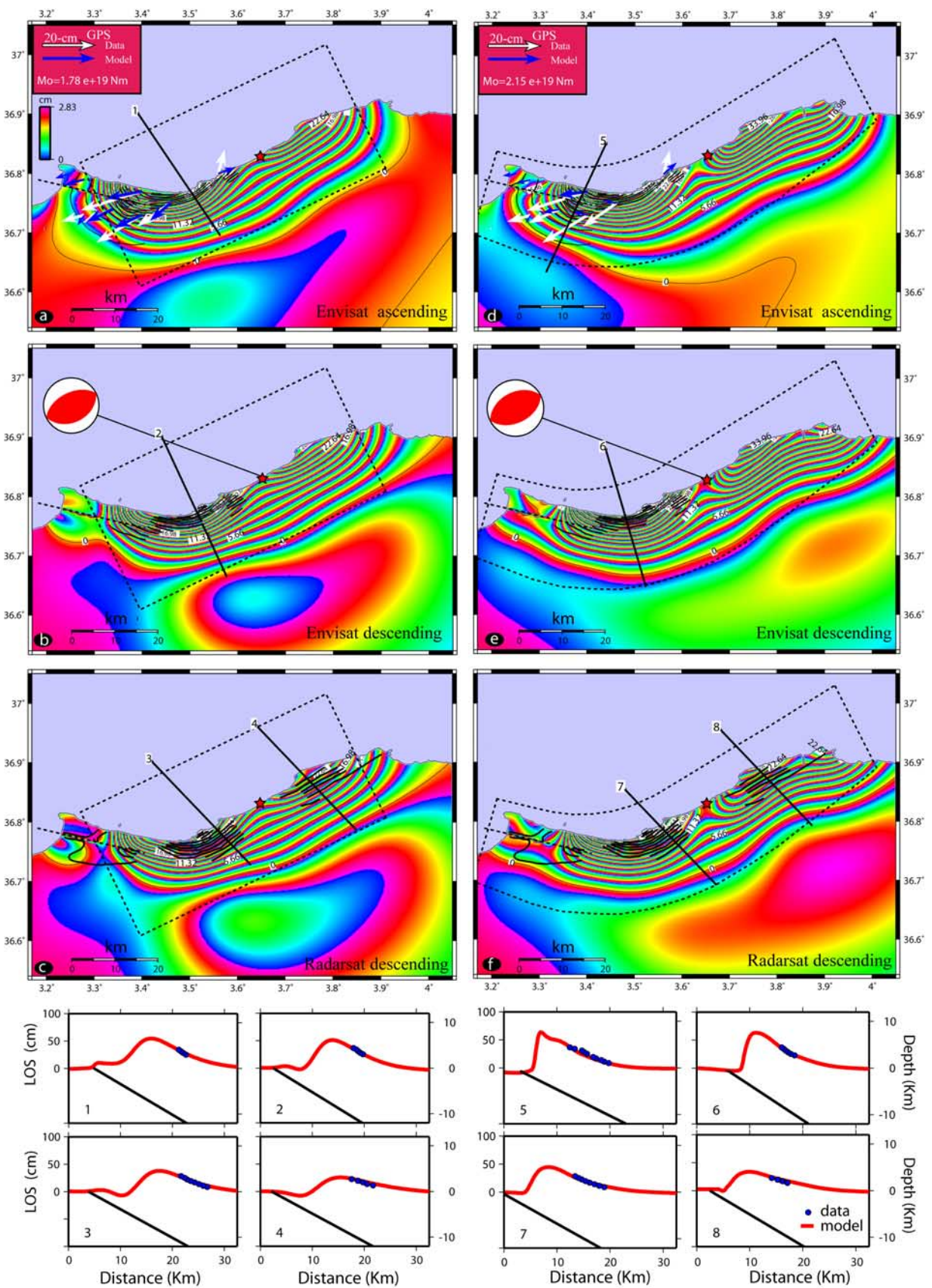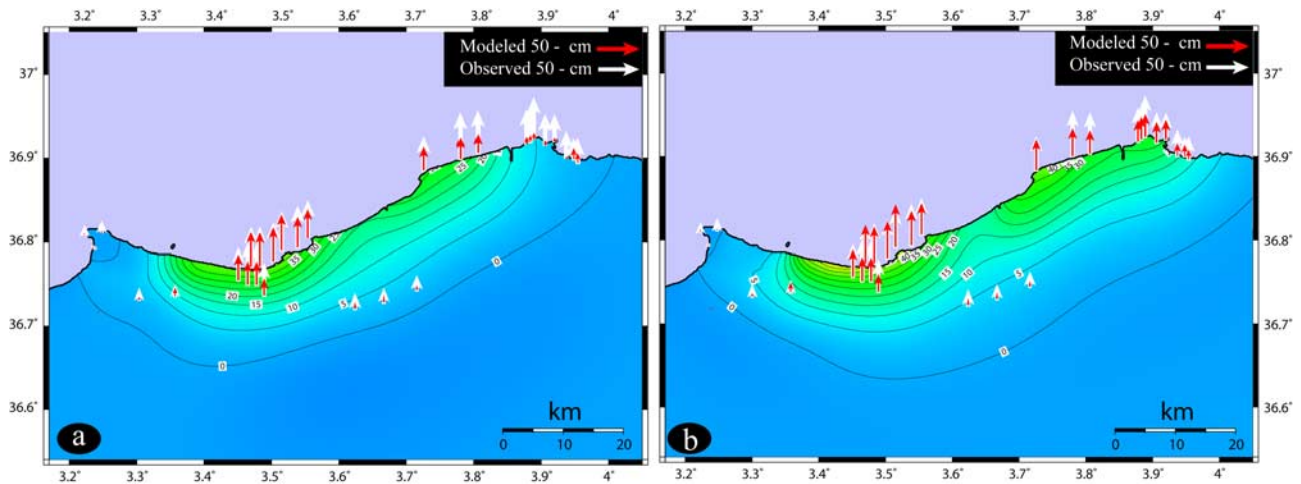
Figure 7

Figure 8. Vertical component of surface displacement (contour lines in cm) predicted by the preferred models for the (a) planar and (b) curved faults. Note that the curved fault solution better explains the uplift measurements east of Cap Djenet.

7c) and curved (Figures 7d–7f) faults, together with the observed fringes (black lines) for comparison. The main features of the observed interferograms are successfully reproduced by the best fit models also illustrated by the LOS profiles (Figure 7). The modeled interferograms also show the difference of surface displacement field (synthetic fringes) with respect to the offshore fault location and dimensions. We also note that the inferred horizontal displacement at the SW end of the planar fault model (Figure 7a) displays a better fit with the coseismic GPS measurements [*Yelles et al.*, 2004]. A comparison between vertical movements obtained from field measurements (coastal uplift and leveling) and the inversion models indicates that the curved fault model provides a much better fit (Figures 8a and 8b). On the other hand, the vertical displacement predicted by the model in Figures 8a and 8b is in good agreement and within the error range (±0.10 m) of the uplift measurements [*Meghraoui et al.*, 2004]. The comparison in Figure 8 also shows that the easternmost modeled uplifts are underestimated for the planar fault model. The inferred geodetic moments of 1.78×10^{19} N m (M_w 6.8) and 2.15×10^{19} N m (M_w 6.8) determined from the inversion models are, however, comparable and in good agreement with those obtained from seismological observations (Table 2). The remaining fringes in the residual interferograms of Figures 9a, 9b, 9c, 9d, 9e, and 9f and in particular for RADARSAT may result from atmospheric artifacts and unaccounted complexity of the rupture geom-

etry, especially around the western termination of the earthquake rupture where the Blida, Thenia and Zemmouri faults meet (Figure 1b).

5. Discussion and Conclusion: Constraints of a Hidden Thrust by InSAR Along a Coastal Area

[18] The crustal deformation associated with the coastal 2003 Zemmouri earthquake is documented using the InSAR analysis combined with uplift measurements and GPS data. The surface displacements obtained by the InSAR, coastal uplift and GPS measurements on a maximum of 20-km-wide strip along the coastline helped us to constrain the rupture geometry and its location offshore. The fringes observed on the Envisat and RADARSAT interferograms of the earthquake area provide an important data set for the modeling of the fault rupture. The two inversion models of surface displacements provide geodetic moments of 1.78×10^{19} N m (M_w 6.8) and 2.15×10^{19} N m on a 30° to 50° SE dipping fault rupture whose tip is located at ~8 to 18 km offshore from the coastal epicenter (Figures 5a and 5b). Our modeling clearly suggests an offshore N60°–65° trending fault rupture, dipping 40° to 50° SE and located at about 8 to 13 km from the coast (Figures 5 and 8). The seismic moment, fault geometry and slip distribution are in good agreement with the main shock and aftershock distribution and teleseismic waveform modeling (Table 2) [*Bounif et al.*, 2004; *Delouis et al.*, 2004; *Ayadi et al.*, 2008].

Figure 7. Synthetic fringes obtained from the inversion of the digitized fringe lines (in black as in Figures 4e, 4f, and 4g) obtained from Envisat ascending and descending, and (a, b, and c) RADARSAT descending for the planar fault and (d, e, and f) curved fault. Dashed rectangle represents the modeled fault area. The fringe pattern is labeled with LOS displacement in cm (white box). Numbered LOS profiles on maps are indicated below. The dotted black line to the west is the Thenia fault. The red star is the relocated main shock epicenter [*Bounif et al.*, 2004]. (left) The planar fault model predicts horizontal surface slip (blue arrows) in agreement with GPS measurements (white arrows [*Yelles et al.*, 2004]) except for the northward vector immediately west of the epicenter. (right) The curved fault model also provides a good fit with the GPS directions, but the amount of measured displacements is larger. The geodetic moment (top left corner) obtained from inversion of InSAR, uplift, and GPS data is consistent with those obtained from seismology (Table 2).
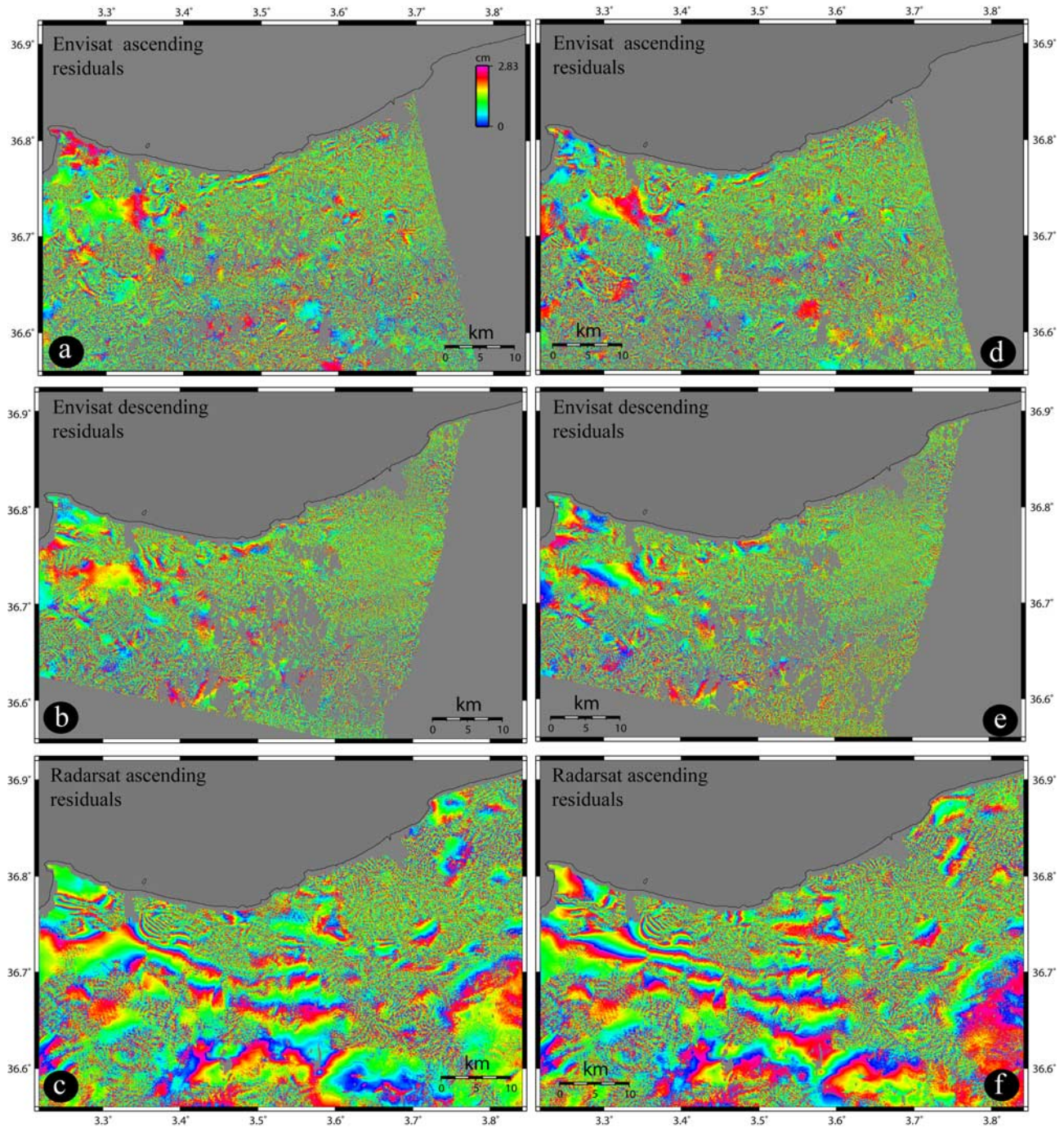
Figure 9. Residual interferograms (a, b, and c) for planar fault model and (e, f, and g) for the curved fault model obtained after subtracting the synthetic interferograms (Figure 7) from the observed data (Figures 4a, 4b, 4c, and 4d). The residuals are negligible for Envisat interferograms but more significant in the case of RADARSAT interferograms probably due to atmospheric artifacts and unaccounted complexity of the rupture geometry. Reference of SAR images is in top left corner.

5.1. InSAR Resolution and Sensitivity

[19] Although atmospheric noise and low coherence in RADARSAT images hampered the quality of interferograms, coseismic fringes are still visible by patches in the Boumerdes and Cap Djenet-Dellys areas (Figure 4). The lack of information on surface deformation in interferograms near the epicenter zone and areas of low coherence led to some difficulties to recognize the nominal deformation. Nevertheless, field investigations of coastal uplift measured with tape, leveling and DGPS [*Meghraoui et al.*, 2004] and GPS measurements [*Yelles et al.*, 2004] correlated with the fringe distribution contribute to better resolve uncertainties of the surface deformation. Although the InSAR data cover a period of ∼1 year for RADARSAT
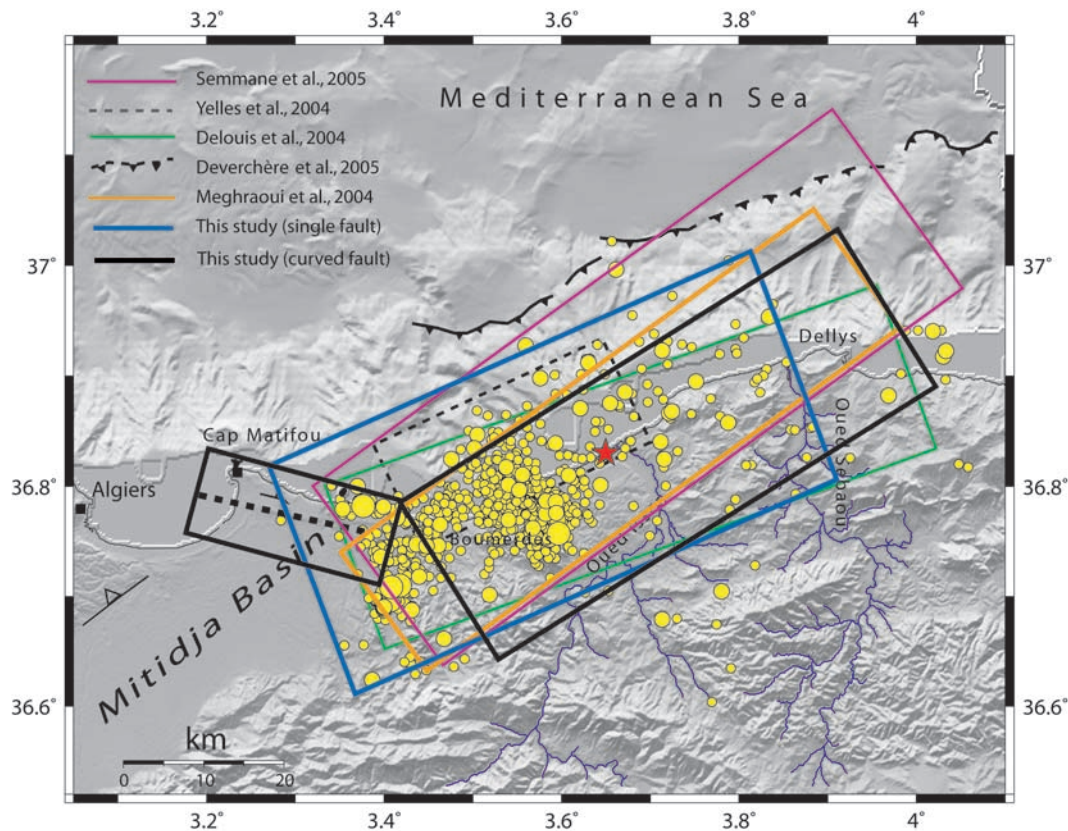
Figure 10. Location and dimension of 2003 Zemmouri earthquake fault rupture from different models and authors (see text for explanation). The red star is the relocated epicenter [*Bounif et al.*, 2004], and the aftershock distribution is from *Ayadi et al.* [2008]. The N105° trending dashed line south of Cap Matifou corresponds to the nearly vertical Thenia fault. Our planar fault model (blue rectangle) and curved fault model (black rectangles, see also Figures 5 and 6) comply with the InSAR, coastal uplift, and GPS data and take into account the large coverage of InSAR data in the earthquake area.

and ~4 months for Envisat (Table 2), the interferograms reflect mainly the coseismic deformation. Indeed, postseismic slip obtained from GPS measurements in the earthquake area indicates ~1 cm/a between 2003 and 2006 [*Mahsas et al.*, 2008] and do not add a significant displacement in interferograms. The locally inverted fringes visible in RADARSAT interferograms about 10 km WSW of Boumerdes may be interpreted as a local artifact possibly due to water pumping for agricultural purposes in the Mitidja Quaternary basin. However, the consistent fringe distribution in the SW end of the earthquake rupture zone may include surface displacement due to the main aftershocks of 27 May (M_w 5.8), 28 May (M_w 4.9), and 29 May (M_w 5.0, Figure 2). In comparison with other case studies of InSAR applied to small surface deformation [*Lohman and Simons*, 2005; *Belabbes et al.*, 2008], these moderate and shallow main aftershocks may in fact generate 3 to 5 fringes in addition to the main shock coseismic surface deformation.

5.2. Fault Geometry and Surface Deformation

[20] The integration of InSAR data with coastal uplift and GPS results combined with the main shock and aftershock study [*Ayadi et al.*, 2008] constrains the 2003 earthquake fault location, dimension and geometry at depth. The 2003 earthquake rupture is hidden by the sea and although the

surface deformation measured inland infers only a partial picture of the fault rupture, our modeling suggest that the fault rupture may have reached the seafloor ~8 to 18 km north of the epicenter (Figures 5a and 5b). However, the lowest RMS errors (<2.7 cm) suggest surface faulting between ~8 and 13 km offshore from the epicenter on a 40° to 50° SE dipping fault rupture (Figures 5 and 10). Using several fault dips, the RMS misfits of Figures 5a and 5b show a clear difference between the planar fault model (Figure 5a) and the curved fault model (Figure 5b). Using the tomographic analysis of the main shock and aftershocks distribution, the N60°–65° trending and 40° to 50° SE dipping rupture geometry illustrate the fault plane at depth and related seafloor rupture at a distance <10 km offshore (Figure 11) [*Ayadi et al.*, 2008]. The fixed N54° strike and ~15 km distance of the fault rupture from the epicenter of *Semmane et al.* [2005] imply that the NE fault section is at a higher distance (>20 km) and do not conform with the significant coastal uplift measured in the Cap Djenet-Dellys region (Figure 3). The inversion of seismic waveforms combined with geodetic data (coastal uplift and GPS) displays a 40° SE dipping with surface faulting and slip at ~7 to 9 km distance from the epicenter [*Delouis et al.*, 2004]. The forward modeling of coastal uplift measurements infer a 50° SE dipping fault plane and locate a possible seafloor
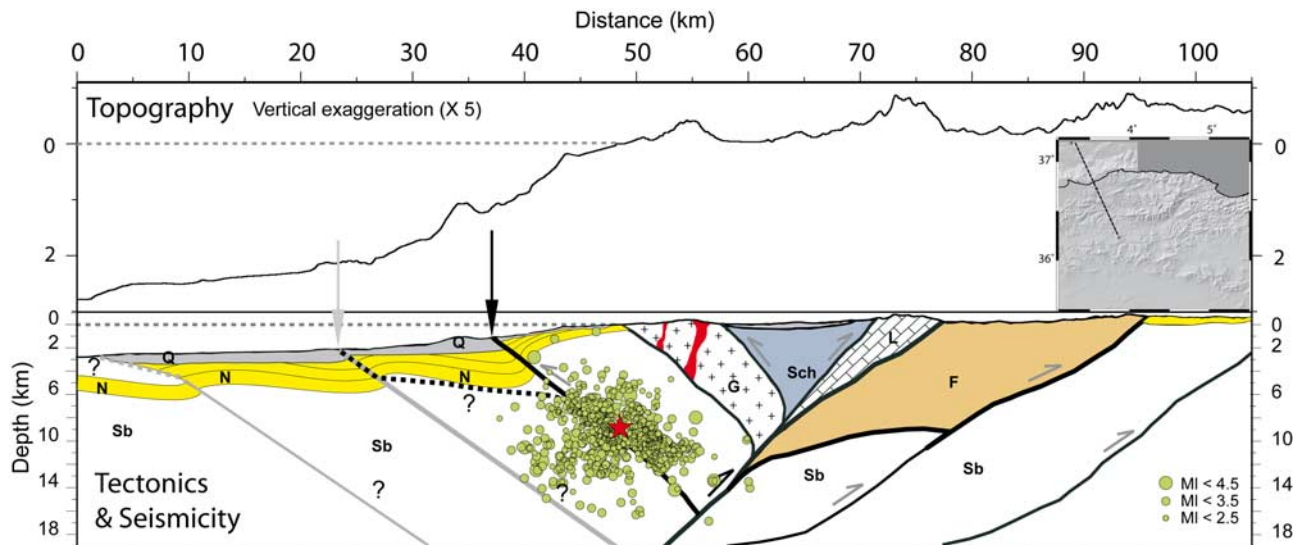
Figure 11. Topographic and geologic sketch across the 2003 earthquake area. Red star is the main shock [*Bounif et al.*, 2004], and green dots are aftershocks [from *Ayadi et al.*, 2008]. Tectonic structures show fold and nappe structures with south verging overthrusts and back thrusts [*Meghraoui*, 1988]. The geological units are made of Paleozoic basement rocks (G for granite and gneiss and Sch for micaschists) with intrusive basaltic units in red (Miocene), Mesozoic and Cenozoic substratum (Sb), Mesozoic and Cenozoic nappes of flyschs (F), Triassic and Jurassic limestones (L), Postnappes Neogene sedimentary basins (N), and Quaternary deposits (Q). The 2003 earthquake fault is well located by the main shock and related aftershocks, and its upward extension indicates the location (black arrow) of a possible fault scarp at ~10 km distance from the epicenter in agreement with the modeled curved fault (see Figures 5b and 6b), the seismic tomography [*Ayadi et al.*, 2008], and the joint inversion of seismological waveforms and geodetic data [*Delouis et al.*, 2004; *Yagi*, 2003]. The gray arrow indicates the possible fault scarp location if we adopt the flat and ramp fault geometry as interpreted from *Déverchère et al.* [2005].

rupture at 5 to 10 km from the epicenter [*Meghraoui et al.*, 2004]. Hence, the joint analysis of geodetic and seismological data constrains the SE dipping fault geometry and rupture location of the 2003 Zemmouri earthquake. The bathymetric survey coupled with seismic profiles offshore (>15 km from the coastline) the earthquake area, locate two outcropping thrusts and related scarps at ~20 and 32 km offshore and infer a flat and ramp fault geometry for the 2003 rupture [*Déverchère et al.*, 2005]. In Figure 10, the seafloor scarps located at the base of the continental slope are scarps B1 and B2 interpreted by *Déverchère et al.* [2005] as the prolongation of 2003 rupture; however, this interpretation that implies a flat and ramp fault geometry (Figure 11) do not take into account the coastal uplift data. If scarps B1 and B2 located at ~20 km from the epicenter are directly related to the 2003 rupture, they imply a slip propagating to the surface and a much higher seismic moment (~M_w 7.3) for the Zemmouri earthquake. In fact, sea bottom rupture scarps at ≥ 15 km distance from the coastline do not match an M_w 6.8 main shock and aftershock location, related coastal uplift and fault models obtained from geodetic data (see fault plane location in Figures 6, 10, and 11).

[21] The SE dipping planar and curviplanar thrust fault models shows two slip patches (Figures 6a and 6b) comparable to the size of thrust segments in the Tell Atlas [*Meghraoui*, 1988] that are likely controlled by the tectonic framework of the eastern Mitidja basin (Figure 1b). The

tectonic background determines the thrust length, strike and dip that control the rupture patches and related size of thrust segments during large and moderate earthquakes. Indeed, surface ruptures of the large El Asnam earthquake (Table 1) displayed 36-km-long thrust fault segment with 6 m maximum surface slip [*Philip and Meghraoui*, 1983]. The maximum slip distribution in the two patches of the Zemmouri earthquake reaches 4.7 m and 2.3 m for the planar and curved fault models, respectively, with surface slip reaching ~0.50 m in the latter. A comparable amount of ~1 m surface slip is also obtained by *Delouis et al.* [2004] and *Semmane et al.* [2005].

5.3. Thenia Fault Branch

[22] To the SW, the 2003 earthquake rupture propagation suggests a fault interaction and possible reactivation of juxtaposed fault branches and segments that reflect the complex rupture termination. The aftershock distribution showing the WNW-ESE alignment from the tomographic analysis [*Ayadi et al.*, 2008] and the existence of surface cracks along the Thenia fault suggested the idea of a curved fault model. Indeed, the bilateral rupture propagation obtained from body wave inversion [*Delouis et al.*, 2004] and related maximum slip along the SW fault patch may have terminated against the Thenia fault and induced the N102°E trending surface cracks visible SW of Boumerdes city. The Thenia fault pointed out by the shift of fringes in Figures 4a and 4b is parallel to the aftershocks alignment as

clearly shown in the tomography of the western fault section [see *Ayadi et al.*, 2008, Figures 2 and 3]. The Thenia fault and parallel fault branches can be considered as tear faults that accommodate the northwest thrust fault propagation with regards to the Blida thrust system (Figure 1b). The Thenia fault branches may also act as a barrier and explain the arrest of the lateral rupture propagation during the 2003 earthquake.

5.4. Thrust Ruptures and Geometrical Complexities

[23] Other blind or hidden thrust fault structures show comparable pattern of surface deformation and rupture geometry at depth with structural control of slip distribution and size of fault patches [*Stein and Yeats*, 1989]. The 10 October 1980 El Asnam earthquake (M_s 7.3) revealed ~36-km-long thrust surface ruptures with three main segments striking NE to ENE pointing out the complex rupture geometry at depth of seismogenic faults in the Tell Atlas [*Philip and Meghraoui*, 1983; *Chiarabba et al.*, 1997]. The 2 May 1983 Coalinga earthquake (M_s 6.5) and related parallel fault branches to the San Andreas fault took place on the 65° NE dipping reverse fault geometry inferred by the surface deformation and related surface folding [*Stein and King*, 1984]. The 6 May 1976 Friuli earthquake (M_s 6.5, Alpine belt in NE Italy) also shows complex thrust faulting with two ~30° NNE dipping parallel patches with blind to semiblind earthquake ruptures and a structural control of the fault propagation [*Aoudia et al.*, 2000]. More recently, the subpixel analysis of SAR images of the 8 October 2005 Kashmir earthquake (M_w 7.6) area indicates slip distribution on a ~31° NE dipping thrust fault with three main segments where the rupture initiation and arrest are on intersecting faults [*Pathier et al.*, 2006]. In our case, the aftershocks analysis of the 2003 Zemmouri earthquake indicates in cross sections en echelon SE dipping fault segments separated by a 3-km-wide step over [*Ayadi et al.*, 2008]. From the seismic moment tensor of main shock and aftershocks, *Braunmiller and Bernardi* [2005] suggest a NNE trending transform fault that limits the SW rupture. The focal mechanism solution of the 29 May 2008 (M_w 5.0) aftershock shows a high-angle NNE trending nodal fault plane and may be interpreted as a transform fault at a step over between the 2003 earthquake rupture farther NE and the Blida thrust system to the SW (Figure 1b). However, the inferred transform fault inland shows no evidence of InSAR signature comparable to that of the Thenia fault.

5.5. Seismic Hazard Implications

[24] Our study shows that an InSAR analysis along a coastal region is able to provide useful constraints on an earthquake rupture area and associated seismic hazard on neighboring fault segments (Figure 1b). Moreover, the Mitidja basin displays to its northern edge the Sahel anticline that hides a 70-km-long NW dipping thrust fault in which the westernmost section was reactivated during the 1989 Tipaza earthquake (M_w 5.9 [*Meghraoui*, 1991]) (Figure 1b). The fact that the two edges of the basin were recently reactivated suggests that the central sections of either the Sahel anticline or the Blida thrust fault system must accommodate shortening movements. The InSAR analysis and modeling of the 2003 Zemmouri earthquake rupture allow us to constrain the SW rupture termination and may

contribute to a better seismic hazard evaluation. The possible generation of a future $M_w \geq 7$ earthquake farther west along the nearby Blida or Sahel thrust fault segments that limit the Mitidja basin (Figure 1b) put the Algiers city and population at high seismic risk.

References

Akoglu, A. M., Z. Cakir, M. Meghraoui, S. Belabbes, S. O. El Alami, S. Ergintav, and S. Akyüz (2006), The 1994−2004 Al Hoceima (Morocco) earthquake sequence: Conjugate fault ruptures deduced from InSAR, *Earth Planet. Sci. Lett.*, *252*, 467−480, doi:10.1016/j.epsl.2006.10.010.

Alasset, P. J., H. Hébert, S. Maouche, V. Calbini, and M. Meghraoui (2006), The tsunami induced by the 2003 Zemmouri earthquake (M_w = 6.9, Algeria); modelling and results, *Geophys. J. Int.*, *166*, 213−226, doi:10.1111/j.1365-246X.2006.02912.x.

Aoudia, K., A. Sarao, B. Bukchin, and P. Suhadolc (2000), The 1976 Friuli (NE Italy) thrust earthquake: A reappraisal 23 years later, *Geophys. Res. Lett.*, *27*, 573−576, doi:10.1029/1999GL011071.

Ayadi, A., et al. (2003), Strong Algerian earthquake strikes near capital city, *Eos Trans. AGU*, *84*, 561−568.

Ayadi, A., C. Dorbath, F. Ousadou, S. Maouche, M. Chikh, M. A. Bounif, and M. Meghraoui (2008), Zemmouri earthquake rupture zone (M_w 6.8, Algeria): Aftershocks sequence relocation and 3-D velocity model, *J. Geophys. Res.*, *113*, B09301, doi:10.1029/2007JB005257.

Belabbes, S., M. Meghraoui, Z. Cakir, and Y. Bouhadad (2008), InSAR analysis of a blind thrust rupture and related active folding: The 1999 Ain Temouchent earthquake (M_w 5.7, Algeria) case study, *J. Seismol.*, doi:10.1007/s10950-008-9135-x.

Bounif, A., et al. (2004), The 21 May 2003 Zemmouri (Algeria) earthquake M_w 6.8; relocation and aftershock sequence analysis, *Geophys. Res. Lett.*, *31*, L19606, doi:10.1029/2004GL020586.

Braunmiller, J., and F. Bernardi (2005), The 2003 Boumerdes, Algeria, earthquake; regional moment tensor analysis, *Geophys. Res. Lett.*, *32*, L06305, doi:10.1029/2004GL022038.

Bürgmann, R., P. Rosen, and E. Fielding (2000), Synthetic aperture radar interferometry to measure Earth's surface topography and its deformation, *Annu. Rev. Earth Planet. Sci.*, *28*, 169−209, doi:10.1146/annurev.earth.28.1.169.

Cakir, Z., M. Meghraoui, A. M. Akoglu, N. Jabour, S. Belabbes, and L. Ait-Brahim (2006), Surface deformation associated with the M_w 6.4, 24 February 2004 Al Hoceima, Morocco, earthquake deduced from InSAR: Implications for the active tectonics along North Africa, *Bull. Seismol. Soc. Am.*, *96*, 59−68, doi:10.1785/0120050108.

Chiarabba, C., A. Amato, and M. Meghraoui (1997), Tomographic images of the El Asnam fault zone and the evolution of a seismogenic thrust-related fold, *J. Geophys. Res.*, *102*, 24,485−24,498, doi:10.1029/97JB01778.

Delouis, B., M. Vallée, M. Meghraoui, E. Calais, S. Maouche, K. Lamalli, A. Mahsas, P. Briole, F. Benhamouda, and A. Yelles (2004), Slip distribution of the 2003 Boumerdes-Zemmouri earthquake, Algeria, from teleseismic, GPS, and coastal uplift data, *Geophys. Res. Lett.*, *31*, L18607, doi:10.1029/2004GL020687.

Déverchère, J., et al. (2005), Active thrust faulting offshore Boumerdes, Algeria, and its relations to the 2003 M_w 6.9 earthquake, *Geophys. Res. Lett.*, *32*, L04311, doi:10.1029/2004GL021646.

Domzig, A., et al. (2006), Searching for the Africa-Eurasia Miocene boundary offshore western Algeria (MARADJA'03 cruise), in *Quelques Devel-*

oppements Recents sur la Geodynamique du Maghreb–Some Recent Developments on the Maghreb Geodynamics, pp. 80–91, Elsevier, Paris.

Farr, T. G., et al. (2007), The shuttle radar topography mission, *Rev. Geophys.*, *45*, RG2004, doi:10.1029/2005RG000183.

Fialko, Y., D. Sandwell, D. Agnew, M. Simons, P. Shearer, and B. Minster (2002), Deformation on nearby faults induced by the 1999 Hector Mine earthquake, *Science*, *297*, 1858–1862, doi:10.1126/science.1074671.

Fielding, E. J., T. J. Wright, J. Muller, B. E. Parsons, and R. Walker (2004), Aseismic deformation of a fold-and-thrust belt imaged by synthetic aperture radar interferometry near Shahdad, southeast Iran, *Geology*, *32*, 577–580, doi:10.1130/G20452.1.

Goldstein, R. M., and C. L. Werner (1998), Radar interferogram filtering for geophysical applications, *Geophys. Res. Lett.*, *25*(21), 4035–4038, doi:10.1029/1998GL900033.

Harbi, A., et al. (2007), Macroseismic study of the Zemmouri earthquake of 21 May 2003 (Algeria M_w 6.8), *Earthquake Spectra*, *23*, 315–332, doi:10.1193/1.2720363.

Lohman, R. B., and M. Simons (2005), Locations of selected small earthquakes in the Zagros Mountains, *Geochem. Geophys. Geosyst.*, *6*, Q03001, doi:10.1029/2004GC000849.

Maerten, F., P. Resor, D. Pollard, and L. Maerten (2005), Inverting for slip on three-dimensional fault surfaces using angular dislocations, *Bull. Seismol. Soc. Am.*, *95*, 1654–1665, doi:10.1785/0120030181.

Mahsas, A., K. Lammali, K. Yelles, E. Calais, A. M. Freed, and P. Briole (2008), Shallow afterslip following the 2003 May 21, M_w = 6.9 Boumerdes earthquake, Algeria, *Geophys. J. Int.*, *172*, 155–166, doi:10.1111/j.1365-246X.2007.03594.x.

Massonnet, D., and K. L. Feigl (1998), Radar interferometry and its application to changes in the Earth's surface, *Rev. Geophys.*, *36*, 441–500, doi:10.1029/97RG03139.

Meghraoui, M. (1988), Géologie des zones sismiques du nord de l'Algérie: Paléosismologie, tectonique active et synthèse sismotectonique, Ph.D. dissertation, Univ. Paris-Sud. Orsay, Orsay, France, 356 pp.

Meghraoui, M. (1991), Blind reverse faulting system associated with the Mont Chenoua-Tipaza earthquake of 29 October 1989 (north-central Algeria), *Terra Nova*, *3*, 84–93, doi:10.1111/j.1365-3121.1991.tb00847.x.

Meghraoui, M., and F. Doumaz (1996), Earthquake-induced flooding and paleoseismicity of the El Asnam, Algeria, fault-related fold, *J. Geophys. Res.*, *101*, 17,617–17,644, doi:10.1029/96JB00650.

Meghraoui, M., J. L. Morel, J. Andrieux, and M. Dahmani (1996), Tectonique plio-quaternaire de la chaine tello-rifaine et de la mer d'Alboran; une zone complexe de convergence continent-continent, *Bull. Soc. Geol. Fr.*, *167*, 141–157.

Meghraoui, M., S. Maouche, B. Chemaa, Z. Cakir, A. Aoudia, A. Harbi, P.-J. Alasset, A. Ayadi, Y. Bouhadad, and F. Benhamouda (2004), Coastal uplift and thrust faulting associated with the M_w = 6.8 Zemmouri (Algeria) earthquake of 21 May 2003, *Geophys. Res. Lett.*, *31*, L19605, doi:10.1029/2004GL020466.

Nocquet, J. M., and E. Calais (2004), Geodetic measurements of crustal deformation in the western Mediterranean and Europe, *Pure Appl. Geophys.*, *161*, 661–681, doi:10.1007/s00024-003-2468-z.

Ouyed, M., M. Meghraoui, A. Cisternas, A. Deschamps, J. Dorel, J. Fréchet, R. Gaulon, D. Hatzfeld, and H. Philip (1981), Seismotectonics of the El Asnam earthquake, *Nature*, *292*, 26–31, doi:10.1038/292026a0.

Pathier, E., E. Fielding, T. Wright, R. Walker, B. Parsons, and S. Hensley (2006), Displacement field and slip distribution of the 2005 Kashmir earthquake from SAR imagery, *Geophys. Res. Lett.*, *33*, L20310, doi:10.1029/2006GL027193.

Philip, H., and M. Meghraoui (1983), Structural analysis and interpretation of the surface deformations of the El Asnam earthquake of October 10, 1980, *Tectonics*, *2*, 17–49, doi:10.1029/TC002i001p00017.

Resor, P. G., D. D. Pollard, T. J. Wright, and G. C. Beroza (2005), Integrating high-precision aftershock locations and geodetic observations to model coseismic deformation associated with the 1995 Kozani-Grevena earthquake, Greece, *J. Geophys. Res.*, *110*, B09402, doi:10.1029/2004JB003263.

Scharroo, R., and P. Visser (1998), Precise orbit determination and gravity field improvement for the ERS satellites, *J. Geophys. Res.*, *103*, 8113–8127, doi:10.1029/97JC03179.

Semmane, F., M. Campillo, and F. Cotton (2005), Fault location and source process of the Boumerdes, Algeria, earthquake inferred from geodetic and strong motion data, *Geophys. Res. Lett.*, *32*, L01305, doi:10.1029/2004GL021268.

Serpelloni, E., G. Vannucci, S. Pondrelli, A. Argnani, G. Casula, M. Anzidei, P. Baldi, and P. Gasperini (2007), Kinematics of the western Africa-Eurasia plate boundary from focal mechanisms and GPS data, *Geophys. J. Int.*, *169*, 1180–1200, doi:10.1111/j.1365-246X.2007.03367.x.

Stein, R., and G. King (1984), Seismic potential revealed by surface folding: 1983 Coalinga, California, earthquake, *Science*, *224*, 869–872, doi:10.1126/science.224.4651.869.

Stein, R., and R. Yeats (1989), Hidden earthquakes: Large earthquakes can take place not only on faults that cut the Earth's surface but also on "blind" faults under folded terrain, *Sci. Am.*, *260*(6), 48–57.

Stich, D., C. J. Ammon, and J. Morales (2003), Moment tensor solutions for small and moderate earthquakes in the Ibero-Maghreb region, *J. Geophys. Res.*, *108*(B3), 2148, doi:10.1029/2002JB002057.

Thomas, A. L. (1993), A three-dimensional, polygonal element, displacement discontinuity boundary element computer with applications to fractures, fault, and cavities in the Earth's crust, Master's thesis, 221 pp., Stanford Univ., Stanford, Calif.

Wessel, P., and H. F. Smith (1998), New, improved version of the Generic Mapping Tools released, *Eos Trans. AGU*, *79*, 579, doi:10.1029/98EO00426.

Wright, T. J., Z. Lu, and C. Wicks (2004), Constraining the slip distribution and fault geometry of the M_w 7.9, 3 November 2002, Denali fault earthquake with interferometric synthetic aperture radar and Global Positioning System data, *Bull. Seismol. Soc. Am.*, *94*, S175–S189, doi:10.1785/0120040623.

Yagi, Y. (2003), Source process of large and significant earthquakes in 2003, *Bull. Int. Inst. Seismol. Earthquake Eng.*, special volume, 145–153.

Yelles, K., K. Lammali, A. Mahsas, E. Calais, and P. Briole (2004), Coseismic deformation of the May 21st, 2003 earthquake, Algeria, from GPS measurements, *Geophys. Res. Lett.*, *31*, L13610, doi:10.1029/2004GL019884.

Yielding, G., M. Ouyed, G. C. P. King, and D. Hatzfeld (1989), Active tectonics of the Algerian Atlas mountains—Evidence from aftershocks of the 1980 El Asnam earthquake, *Geophys. J. Int.*, *99*(3), 761–788, doi:10.1111/j.1365-246X.1989.tb02057.x.

Zebker, H. A., J. F. Vesecky, and Q. Lin (1994), Phase wrapping through fringe-line detection in synthetic aperture radar interferometry, *Appl. Opt.*, *33*, 201–208.

————————————

S. Belabbès and M. Meghraoui, Institut de Physique du Globe de Strasbourg, UMR 7516, 5, rue Rene Descartes, F-670084 Strasbourg, France. (mustapha.Meghraoui@eost.u-strasbg.fr)

Z. Çakir, Faculty of Mines, Istanbul Technical University, 34469 Maslak, Istanbul, Turkey.

C. Wicks, U.S. Geological Survey, 345 Middlefield Road, MS 977, Menlo Park, CA 94025, USA.